IrIII-pyridoannelated N-heterocyclic carbene complexes: potent theranostic agents via mitochondria targeting

Anna Bonfiglio, Conor Mccartin, Ulises Carrillo, Cristina Cebrian, Philippe Gros, Sylvie Fournel, Antoine Kichler, Chantal Daniel, Matteo Mauro

IrIII-pyridoannelated N-heterocyclic carbene complexes: potent theranostic agents via mitochondria targeting

Anna Bonfiglio,[a],+ Conor McCartin,[b],+ Ulises Carrillo,[c] Cristina Cebrián,[c] Philippe C. Gros,[c] Sylvie Fournel,[b] Antoine Kichler,[b] Chantal Daniel,[d] and Matteo Mauro,[a],*

[a] MSc. A. Bonfiglio, Dr. M. Mauro, Institut de Physique et Chimie des Matériaux de Strasbourg (IPCMS) UMR7504, Université de Strasbourg & CNRS, 23 rue du Loess, 67083 Strasbourg (France)
E-mail: mauro@unistra.fr
Homepage: http://www.ipcms.unistra.fr/?page_id=31293
[b] MSc. C. McCartin, Dr. A. Kichler, Prof. S. Fournel, 3Bio Team, CAMB UMR7199 , CNRS−University of Strasbourg, Faculté de Pharmacie 74 route du Rhin, F-67401 Illkirch cedex, France.
[c] MSc. U. Carrillo, Dr. C. Cebrián, Dr. P. C. Gros, Université de Lorraine, CNRS, L2CM, F-57000 Metz, France
[d] Dr. C. Daniel, Laboratoire de Chimie Quantique, Institut de Chimie de Strasbourg UMR7177, Université de Strasbourg-CNRS 4 Rue Blaise Pascal, 67000 Strasbourg (France)
E-mail: c.daniel@unistra.fr
+ *These authors contributed equally to the work.*

Abstract: A novel family of Ir^{III} complexes bearing a pyridoannelated N-heterocyclic carbene is herein described. The target compounds **1–5** are straightforwardly prepared and fully characterized. Comprehensive investigation of their optical properties reveals a rare case of dual emission ascribed to two excited states localized onto different portions of the molecule, as confirmed by both optical spectroscopy and time-dependent density functional calculations including spin-orbit coupling. The cytotoxicity against cancer cell lines is investigated as well. Remarkably, **2–5** show up to 50-fold higher anticancer activity *in vitro* compared to oxaliplatin market drug with concentration values required to reduce by 50% the cell viability (IC_{50}) in the low μM range. Finally, in-depth biological investigation on the most cytotoxic compound **4** reveals its powerful mitochondrial dysfunctioning activity and efficient reactive oxygen species production, associated with apoptosis as the mechanism of cell death.

Introduction

Since the discovery of cisplatin in 1965, platinum compounds have remained a mainstay of cancer chemotherapy.[1] However, despite the development of second and third generation platinum compounds, severe side effects and drug resistance remain problematic in their usage.[2] In particular, their mechanism of action - which consists in the induction of cell death via the generation of genomic adducts - is susceptible to interference at several points, via up- or down-regulation of anti- or pro-apoptotic proteins, respectively.[3] Thus, the continued development of metal-based anti-cancer complexes, which may overcome these adverse effects and chemo-resistance, is currently of great clinical interest. In this respect, major attention is devoted to compounds capable of interfering with mitochondrial function due to their ability to by-pass apoptotic resistance mechanisms through direct induction of the intrinsic (*i.e.* mitochondrial mediated) apoptosis pathway.[4] Promising anti-cancer activity is to be found among compounds of several other metals including gold, silver, copper, palladium, ruthenium, rhodium, iron and rhenium.[5] Cyclometalated Ir^{III} complexes are of particular interest since they can combine biological activity and excellent and highly tuneable photophysical properties.[6] This combination enables their application as *theranostic* agents, *i.e.* simultaneous imaging and therapeutic properties. Monitoring cellular localization of exogenous metallodrugs upon internalization via optical techniques is of paramount importance for elucidating the mechanism of action and establishing structure-properties relationships without the need of chemical modification of the drug, which may perturb the activity of this latter. Furthermore, it is well established that both optical properties and biological activities are largely influenced by the nature of the coordinated ligands, also playing key role in the (photo-)chemical stability and cellular localization of the final metal complex. Hence, judicious choice of coordination sphere is of pivotal importance for the activity of this class of photo- and bio-active organometallic compounds.

N-heterocyclic carbenes (NHCs) are an outstanding class of ligands featuring peculiar characteristics, such as strong σ-donating and weak to moderate π-accepting properties. As such, they have come to prominence in the field of organometallics,[7] since their first attempts of isolation as stable species[8]. Currently, they find useful applications in several fields including molecular catalysis,[9] materials science,[10] and more recently in bio-medicine, for the development of biologically active compounds with potent anti-bacterial and anti-cancer effects[11,12]. Indeed, the presence of NHCs is advantageous for biological applications of metallodrugs due to the stability of the metal-carbene bond, and in the facile chemical modifications at both backbone and wingtip positions that enable straightforward tuning of both steric and electronic features.[13]

The first examples of luminescent Ir^{III}-NHC complexes with anticancer activity were reported by Mao and co-workers, to the best of our knowledge.[14] The first series of compounds belong to the family of phenylpyridine-based cyclometalated Ir^{III} with general formula $[Ir(ppy)_2(bis\text{-NHC})]Cl$, where ppy is the 2-phenylpyridine.[14a] The *in vitro* toxicity tested after 48 hours of incubation of the complexes showed good to high activities against different human cancer and healthy cell lines via mitochondria targeting. More recently, the same group expanded upon the series describing two novel Ir^{III}-NHC displaying near infrared (NIR) emission achieved through extension of the π-aromatic system of the cyclometalating ligand.[14b] Similarly to their congeners, the compounds were found

to specifically localize into mitochondria and able to efficiently induce cell death via the mitochondrial pathway. Independently, Che and co-workers investigated related Ir-NHC complexes of the family $[Ir(C^N)_2(bis\text{-}NHC)]^+$, where C^N is phenylpyridine-type of ligands. They found out that such complexes are highly cytotoxic against HeLa cell line, but compounds accumulated selectively into the endoplasmic reticulum (ER) instead.[15] Moreover, Liu and co-workers explored anti-cancer activity of Ir^{III}-ppz complexes, where ppz = 1-phenylpyrazole, bearing an imine-N-heterocyclic carbene ancillary ligand.[16] Nevertheless, these four series of Ir^{III}-NHC complexes share the same N-alkylated imidazol-2-ylidene scaffold, and effect of electronic and structural variation at the NHC site was not explored to date.

We aim at investigating Ir^{III}-NHC complexes that combine enhanced cytotoxicity with suitable properties and gaining deeper understanding of structure-properties relationship in this class of metallodrugs. Therefore, we questioned about the impact of the introduction of an annulated aromatic ring onto the ancillary NHC moiety toward tumour cell killing activity of this class of compounds. Herein, we describe a novel series of luminescent Ir^{III} complexes bearing a pyridyl-pyridoannulated NHC ancillary ligand and varying the cyclometalating chelate. Their optical properties are presented and rationalized also with the help of computational approaches. Finally, the biological activity of this novel class of Ir^{III}-NHC complexes is thoroughly evaluated showing potent anti-tumoral activity and demonstrating appealing application for these compounds as theranostic agents.

Results and Discussion

Synthesis

The general synthetic pathway employed for the preparation of the cyclometalated $[Ir(C^N)_2(pyipy)]PF_6$ complexes and the chemical structure of the target complexes **1**–**5** is depicted in Scheme 1 and Scheme 2, respectively. The ^1H, ^{19}F and ^{13}C NMR as well as the HR-ESI-MS spectra of the target complexes are displayed in Figure S1–S30 of the Supplementary Information. The synthesis starts with deprotonation at C(3) position of the 2-(2-pyridyl)imidazo[1,5-*a*]pyridinium hexafluorophosphate procarbenic ligand, namely $[pyipy]PF_6$, via Ag_2O-supported C–H bond activation yielding the formation of the annelated NHC ligand following the original procedure reported by Lassaletta.[17] Subsequently, transmetallation reaction was carried out *in situ* by adding the corresponding chloro-bridged iridium dimer. These latter were prepared using the classical procedure reported previously by Nonoyama.[18] Five target complexes **1**–**5** bearing different cyclometalating C^N ligands were obtained in moderate yields after purification.

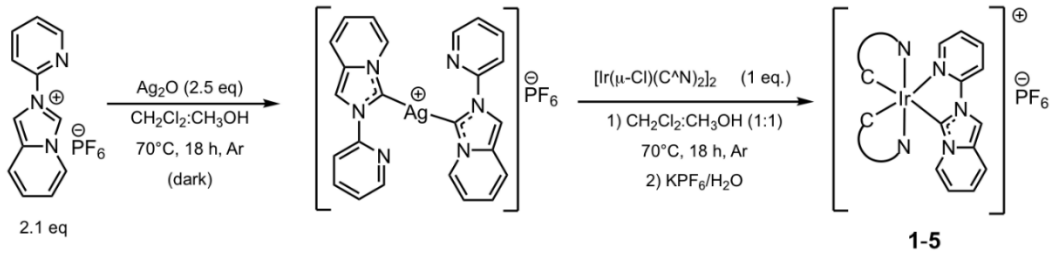

Scheme 1. Schematic synthetic pathway used for the synthesis of complexes **1**–**5**.

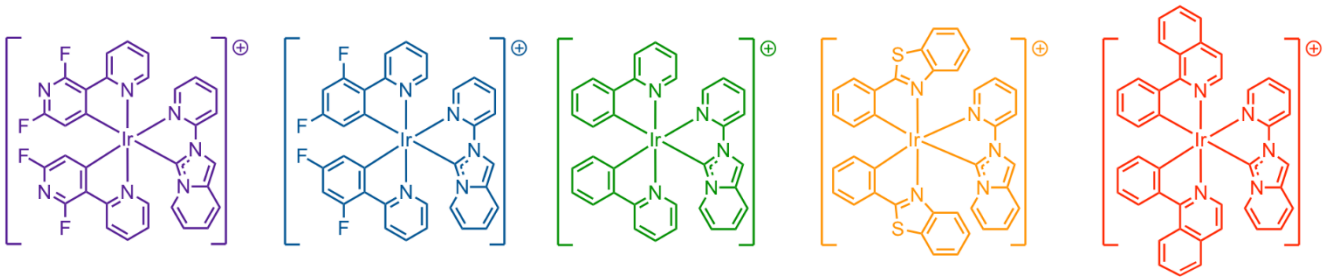

Scheme 2. Chemical structure of the Ir^{III} complexes **1**–**5** investigated herein. All the complexes were prepared as PF_6^- salt.

For derivative **3** the chemical connectivity and the solid-state packing was unambiguously determined by solving the single crystal structure by means of X-ray diffractometric analysis (see Figure 1). Expectantly, the iridium atom is coordinated within a distorted octahedral geometry by two cyclometalating C^N ligand arranged in a *trans*-N,N fashion and a pyipy carbene ligand. As far as complex **3** is concerned, Ir–N bonds are in the range 2.05–2.18 Å in agreement with related complexes.[19] Notably, while the Ir–C(34) bond located in *trans* to the pyridine of the pyipy is within the expected range of distances, Ir–C(7) and Ir–C(23) bond lengths display longer values due to the strong *trans* influence exerted by the cyclometalating phenyl and carbene ring, respectively, located in mutually *trans* position. The refinement parameters and a more exhaustive list of geometrical data are listed in Table S1 and S2 of the Supplementary Information, respectively.

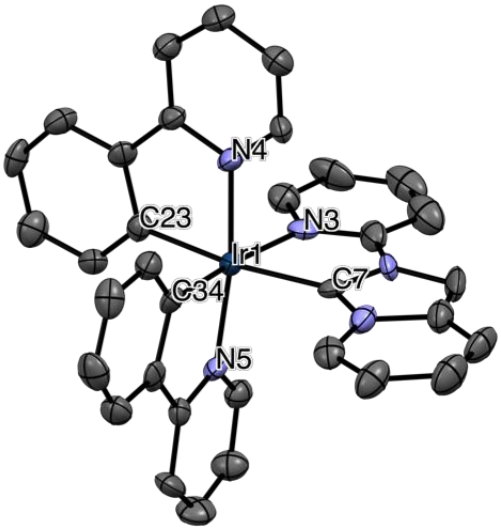

Figure 1. ORTEP diagram of compound **3** with thermal ellipsoids shown at 50% probability level obtained by single-crystal X-ray diffractometric analysis. Hydrogen atoms and PF_6^- anion are omitted for clarity. Selected bond lengths (Å): Ir–C(7) = 2.072(9) Å; Ir–C(23) = 2.048(9) Å; Ir–C(34) = 1.995(9) Å; Ir–N(3) = 2.181(8) Å, Ir–N(4) = 2.053(7) Å, Ir–N(5) = 2.065(7) Å.

Photophysical characterization

The electronic absorption and photoluminescence spectra recorded for samples of complexes **1**–**5** in CH_2Cl_2 solution at a concentration of 3×10^{-5} M at room temperature are displayed in Figure 2. The corresponding steady state and time-resolved photophysical data are summarized in Table 1.

In the higher energy region (λ_{abs} <350 nm) the electronic absorption spectrum is characterized by intense (ε = *ca.* 1–4×10^4 M^{-1} cm^{-1}) bands that can be ascribed to the intraligand transition of π-π* character localized onto the C^N ligand, namely $^1IL_{C^N}$. At lower energy, the less intense (ε = *ca.* 0.3–1×10^4 M^{-1} cm^{-1}) and broader bands can be confidentially attributed to overlapping electronic absorption processes arising from different combination of spin-allowed singlet-manifold intraligand charge transfer (^{1}ILCT) and metal-to-ligand charge transfer character (^{1}MLCT). As far as complexes **1**–**2** are concerned, an additional peak is clearly visible in the absorption profile at λ_{max} = 400 (ε = 2.4×10^3 M^{-1} cm^{-1}) and 410 nm (ε = 2.6×10^3 M^{-1} cm^{-1}) for compound **1** and **2**, respectively, attributable to the intraligand absorption involving the ancillary NHC ligand (IL_{NHC}) character, where NHC is the benzannulated pyipy carbene moiety, owing to the sizeable π-extended conjugation of this latter. Expectantly, the lower energy spectrum onset is monotonically shifted towards longer wavelength moving from compound **1** to **5** within the investigated series. This shift is due, on the one hand, to the destabilization of the highest-occupied molecular orbital (HOMO) going from **1** to **2** to **3**; and, on the other hand, to the increased stabilisation of the lowest-occupied molecular orbital (LUMO) going from **3** to **4** to **5** as consequence of the increased π-conjugation of the heteroaromatic ring. These band assignments were also made on the basis of the computational findings (see below) and are also in agreement with related cyclometalated Ir^{III} complexes reported previously.[20]

Upon photo-excitation into the low-lying energy band, dilute samples of complexes **1**–**5** exhibit low to moderate photoluminescence (see Table 1), yet with a dual emission surprisingly. Emission spectrum of compound **1** features one structured band with λ_{em} maxima at 444 and 473 nm, namely high-energy (HE) emission band. In addition, a second structured band is visible on the lower energy (LE) side with λ_{em} at 590 and 648 nm, yet with very low intensity. Moving to complex **2**, the HE band display a bathochromic shift to λ_{em} = 467 nm and 494 nm; whereas, the LE band increases its intensity with no spectral shift apparently. The LE appears even more clearly for compound **3** and the HE band is weak, broad and featureless instead. In complexes **4**–**5**, the stabilization of the π* orbitals imparted by the more extended conjugation of the C^N ligand causes an expected bathochromic shift of the emission profile and band structure is less marked. The different origin of the two emission bands is supported by the independent behaviour observed for the excitation spectra recorded at the HE and LE wavelength (see Figure S31 of the

Supplementary Information) that suggests poor electronic coupling between the two excited states responsible of the dual emission.[21]

As far as complexes **1–3** are concerned, the HE band can be ascribed with confidence to a radiative process arising from a triplet excited state with mainly $^3IL_{C\hat{}N}$ character, although with a partial degree of mixing with the $^1MLCT_{C\hat{}N}$ state depending on the nature of the C^N ligand, as typical of this class of emitters.[20] In particular, for complexes **1**–**2** the sizeable contribution from a $^3IL_{C\hat{}N}$ state is supported by the vibronic profile of the emission spectra with spacing in the order 1100–1400 cm^{-1} attributed to the intraligand C=C and C=N vibrational modes. Furthermore, the formally triplet nature of the emitting state is corroborated by the observed increase of the photoluminescence quantum yield (PLQY) going from air-equilibrated to oxygen-free samples (see Table 1). The compound bearing the unsubstituted ppy ligand, namely complex **3**, displays the lowest (PLQY = 1.3% in degassed CH_2Cl_2 sample) amongst the investigated series; whilst, orange-red emitter **4** possesses the highest PLQY. These findings are in agreement with those reported by Baranoff and co-workers on a related series bearing the 3-methyl-1-(4-methyl-2-pyridyl)benzimidazol-2-ylidene NHC ligand.[20c]

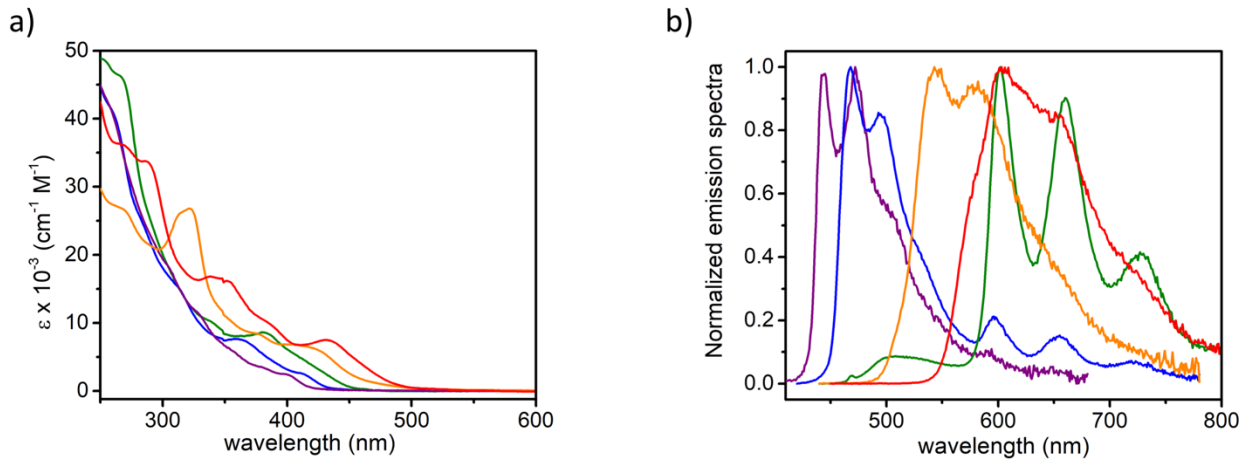

Figure 2. Electronic absorption (*left box*) and photoluminescence spectra (*right box*) of compound **1** (purple traces), **2** (blue traces), **3** (green traces), **4** (orange traces) and **5** (red traces) in CH_2Cl_2 solution at a concentration of 3×10^{-5} M at room temperature. Emission spectra were recorded upon excitation at λ_{exc} = 350 nm for **1**, λ_{exc} = 400 nm for **2**, λ_{exc} = 410 nm for **3**, λ_{exc} = 420 nm for **4** and λ_{exc} = 430 nm for **5**. Spectra of compound **1–5** refer to degassed samples.

It is worth to notice that examples of dual emission in cyclometalated Ir^{III} complexes are scarce and this phenomenon is intriguing also in view of the potential application as broadband emitters.[22] Thus, this finding prompted us to carry out time-resolved emission decay analysis at different emission wavelengths to gain a better understanding of the nature the two emitting excited states. Observed lifetimes fall in the hundreds of nanoseconds to microseconds regime. Also, going from air-equilibrated to degassed samples a sizeable prolongation of the excited-state lifetimes is observed independently of the emission wavelength.

As far as complex **3** is concerned, lifetimes measured for degassed samples at the HE and LE bands display mono-exponential decay with τ_{HE} = 555 ns and τ_{LE} = 6.0 μs, respectively. For complexes **4**–**5**, analysis of the decay traces required a bi-exponential fitting at both shorter and longer wavelength region with similar lifetime components (for examples, τ_1 = 6.1 μs and τ_2 = 1.8 μs for complex **4**), yet with different weights, indicating that the recorded PL profile is composed of two almost overlapping emission bands. Similar results were obtained for complex **2**. The HE band overwhelmed the LE one for complex **1**.

Overall, these findings confirm the mainly triplet nature for both excited states involved in the dual emission process and point towards a $^3MLCT_{C\hat{}N}/^3IL_{C\hat{}N}$ and $^3IL_{NHC}$ character for the HE and LE bands, respectively; the latter state, which possesses poorer emission properties, being responsible of the quenching of the higher-lying $^3MLCT_{C\hat{}N}/^3IL_{C\hat{}N}$ manifold. This picture is also supported by TD-DFT calculation (see below) and agrees well with the experimental data obtained for related luminescent Re(I)-tricarbonyl species bearing the same pyipy NHC ligand that display a $^3LC_{NHC}$ emission with higher energy peak at λ_{em} = 608 nm.[23]

Table 1. Photophysical data recorded for samples of compound **1**–**5** in air-equilibrated and degassed CH_2Cl_2 solution at concentration of 3×10^{-5} M at room temperature.

[a] emission wavelength (in nm) where the lifetime has been recorded at is reported in square brackets.

Cmpd	$\lambda_{max,abs}$ (ε) [nm, (10^3 M^{-1} cm^{-1})]	λ_{em} [nm]	PLQY		τ_{obs}	
			air-equilibrated	*degassed*	*air-equilibrated* [a]	*degassed* [a]
1	306 (17.62), 327 (11.50), 355 (6.03), 380 (3.47), 400 (2.40)	444, 473, 507, 590, 648	1.6%	3.1%	573 ns [443] 504 ns (56%) 65 ns (44%) [641]	1.1 μs [444] 344 ns (21%) 1.5 μs (79%) [641]
2	262 (40.11), 283 (25.03), 313 (15.16), 359 (7.55), 410 (2.63)	467, 494, 596, 654, 720	0.6%	6.2%	139 ns [467] 628 ns (47%) 163 ns (53%) [652]	1.6 μs (35%) 1.3 μs (65%) [467] 7.0 μs (77%) 594 ns (23%) [652]
3	266 (46.28), 309 (15.65), 340 (10.04), 383 (8.55), 420 (3.77)	510, 600, 660, 730	0.1%	1.3%	52 ns (66%) 139 ns (34%) [500] 478 ns [600]	555 ns [500] 6.0 μs [600]
4	322 (26.80), 377(8.37), 420 (6.32), 450 (2.58)	545, 580	1.7%	6.7%	315 ns (65%) 839 ns (35%) [545] 851 ns (33%) 325 ns (67%) [580]	6.1 μs (12%) 1.8 μs (88%) [545] 6.1 μs (12%) 1.8 μs (88%) [680]
5	267 (36.26), 287 (33.71), 344 (16.62), 387 (9.73), 432 (7.49), 460 (3.93)	600, 655	0.6%	4.7%	398 ns (42%) 661 ns (58%) [600] 349 ns (34%) 629 ns (66%) [650]	2.1 μs (20%) 5.9 μs (80%) [600] 2.0 μs (23%) 5.9 μs (77%) [650]

Optical and photophysical properties: theory

The computed time-dependent (TD-DFT) absorption spectra of complexes **1**–**5** are depicted in Figure 3 and the corresponding optimized structures are displayed in Figure S32 along with their geometrical parameters listed in Table S3. The corresponding transition energies without and with SOC as well as computed oscillator strengths are reported in Table S4 and supplementary

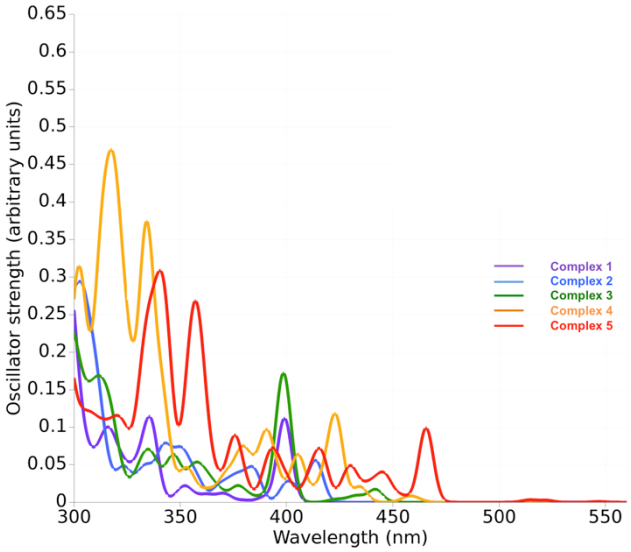

absorption spectra are shown in Figure S33–S34.

Figure 3. TD-DFT absorption spectra of complexes **1–5** computed in CH_2Cl_2 with spin-orbit coupling (SOC).

SOC effects induce an increasing bathochromic shift of the lowest band going from 5 nm (complex **1**) to 73 nm (complex **5**) that follows the character of the low-lying excited states from purely IL_{NHC} states in complexes **1** and **2** to mixed IL/MLCT and LLCT/MLCT in the other compounds. This bathochromic shift is governed by the important singlet/triplet mixing and increases with the $MLCT_{C^N}$/$LLCT_{C^N}$ contributions in the visible energy domain (500–400 nm; complexes **4** and **5**). The most intense peaks are attributed to IL_{C^N} transitions centred at 340–300 nm (complex **4**) and 360–330 nm (complex **5**). The IL_{NHC} excited states calculated at about 390–400 nm in the five complexes are characterized by modest intensities. The Kohn-Sham orbitals involved in the main electronic transitions reported in Table S4 are represented in Figure S35 and the frontier orbitals of the five complexes are depicted in Scheme 3.

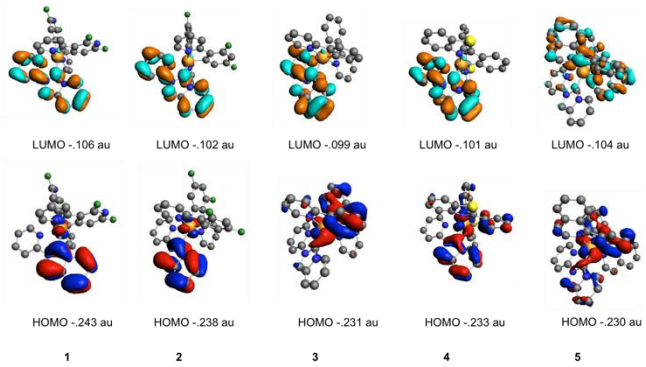

Scheme 3. Kohn-Sham frontier orbitals of complexes **1**–**5** after structure optimization in CH_2Cl_2 at their electronic ground state.

The potentially emissive low-lying triplet excited states T_1–T_3 have been fully optimized (Table S3) and are described in Table 2, which reports their energetics at Franck-Condon (FC) $\Delta E_{S0\text{-}T}$ and after structure optimization, namely their emission computed wavelength (namely λ^{theo}) and the distortion energies ΔE_{dist} needed to reach their minima. The upper triplet states calculated at FC are reported in Table S5.

The lowest triplet manifold (T_1) corresponds to an intraligand (IL_{NHC}) state that is localized onto the NHC moiety and it is calculated at *ca.* 700 nm in the five complexes. It is attainable with a rather large distortion energy (ΔE_{dist} ≥0.25 eV). The low-lying

IL_{C^N} emissive states are mixed with $LLCT_{C^N}$ and $MLCT_{C^N}$ states in T_2 and T_3 and significantly shifted to the red following the prevalence of IL_{C^N} contribution when going from complex **1** to **5**.
The calculated emission wavelengths λ^{theo} reproduce the experimental trends with theoretical maxima at 426 and 508 nm (vs. 444 and 474 nm) in **1**, 451 and 525 nm (vs. 467 and 484 nm) in **2**, 490 and 532 nm (vs. 500 and 540 nm) in **3**, 517 and 571 nm (vs. 545 and 580 nm) in **4** and 582 and 605 nm (vs. 600 and 655 nm) in **5** (Table 1–2). Perturbative spin-orbit correction may improve the theoretical values by 15–20 nm leading to an even better agreement.[24] The distortion energy ΔE_{dist} needed to reach T_3, essentially composed of IL_{C^N} transitions, falls below 0.20 eV in complexes **2**–**5**, both T_2 and T_3 being easily accessible in complex **5** with ΔE_{dist} <0.15 eV. The mixed composition of the low-lying emissive states highlights the sensitivity of the photophysics to both the chemical and surrounding environments.

Table 2. Potentially emissive low-lying triplet excited states of complexes **1**-**5**: character at FC and after structure optimization, calculated vertical transition energies (in eV), $\Delta E_{S0\text{-}T}$ electronic ground state-triplet energy gap, emission wavelength λ^{theo} (in eV and nm) and distortion energy ΔE_{dist} (in eV). The listed data are computed in CH_2Cl_2.

complex	state	character at FC	vertical transition energy [eV]	$\Delta E_{S0\text{-}T}$ [eV]	ΔE_{dist} [eV]	λ^{theo} [eV]	λ^{theo} [nm]	character after structural optimization
1	T_1	IL_{NHC}	2.30	2.07	0.30	1.77	700	IL_{NHC}
	T_2	$MLCT_{C^N}/IL_{C^N}$	3.20	2.81	0.37	2.44	508	IL_{C^N}/ $LLCT_{C^N}$
	T_3	IL_{C^N}/ $MLCT_{C^N}$	3.21	3.13	0.22	2.91	426	$LLCT_{C^N}/IL_{NHC}$/ IL_{C^N}
2	T_1	IL_{NHC}	2.29	2.04	0.29	1.75	708	IL_{NHC}
	T_2	$MLCT_{C^N}/IL_{C^N}$	3.06	2.67	0.31	2.36	525	IL_{C^N} /$MLCT_{C^N}$
	T_3	IL_{C^N}/ $MLCT_{C^N}$	3.09	2.88	0.13	2.75	451	IL_{C^N}/ $MLCT_{C^N}$
3	T_1	IL_{NHC}	2.28	2.03	0.29	1.74	713	IL_{NHC}
	T_2	$LLCT_{NHC}$/ $IL_{C^N}/MLCT_{C^N}$	2.90	2.59	0.26	2.33	532	$MLCT_{C^N}$ /IL_{C^N}/
	T_3	IL_{C^N}/ $MLCT_{C^N}$/ $LLCT_{NHC}$	2.93	2.70	0.17	2.57	482	$MLCT_{NHC}/IL_{NHC}$
4	T_1	IL_{NHC}/ $MLCT_{NHC}$	2.27	2.01	0.28	1.73	717	IL_{NHC}
	T_2	$LLCT_{C^N}$/ $MLCT_{C^N}$	2.72	2.37	0.20	2.17	571	IL_{C^N}/ $LLCT_{C^N}$
	T_3	IL_{C^N}/ $MLCT_{C^N}$/ $LLCT_{C^N}$	2.74	2.53	0.13	2.40	517	$IL_{C^N}/LLCT_{C^N}$

5	T_1	IL_{NHC}/ $LLCT_{C^N}$/ $MLCT_{C^N}$	2.28	2.00	0.26	1.74	713	IL_{NHC}
	T_2	$MLCT_{C^N}$/ IL_{C^N}/ $LLCT_{NHC}$	2.40	2.18	0.13	2.05	605	IL_{C^N}/ $MLCT_{C^N}$
	T_3	IL_{C^N}/ $MLCT_{C^N}$/ $MLCT_{NHC}$/ $LLCT_{NHC}$	2.43	2.20	0.07	2.13	582	IL_{C^N}/$LLCT_{C^N}$

cmpd	log $P_{o/w}$	Pearson co-localisation value
1	0.50	0.48
2	1.26	0.63

Biological evaluation

In vitro cytotoxicity

The *in vitro* cytotoxicity of the compounds was tested against two Human cancer cell lines, HCT116 (human colon carcinoma) and MDA-MB-231 (human breast cancer), by measuring the decrease of NADH and $NADPH^-$ dependant dehydrogenase activity, reflecting a decrease of metabolic activity, using the MTS assay after 24 and 48 hours treatment. The resulting half maximal inhibitory concentration values (concentration required to reduce by 50% the cell viability; IC_{50}) are listed in Table 3 (see also Figures S36–S39 of the Supplementary Information).

Table 3. IC_{50} values (in μM) of the tested complexes **1**–**5**.

Compound	HCT116		MDA-MB-231	
	24 h	***48 h***	***24 h***	***48 h***
1	>50	>50	>50	>50
2	7.2 ± 1.2	2.3 ± 1.4	20.6 ± 2.9	9.2 ± 1.1
3	21.2 ± 4.3	2.1 ± 1.2	16.4 ± 1.2	10.2 ± 1.1
4	7.5 ± 1.1	1 ± 1.1	9.6 ± 1.1	4.8 ± 1.1
5	8.3 ± 1.2	1.7 ± 1.1	13.2 ± 1.2	7.8 ± 1.2
Oxaliplatin	>50	46.57	>50	>50

All IC_{50} values are the mean of at least two independent experiments ± one standard error of the mean (SEM), with each experiment consisting of the mean of three technical replicates. IC_{50} and SEM were calculated by non-linear regression using Prism software.

All the compounds show a similar level of cytotoxicity - of a level much higher than that of the commonly used platinum based anti-cancer compound oxaliplatin - except for compound **1**. Notably, the compounds showed a roughly two- to ten-fold decrease in IC_{50} after 48 hours - reaching IC_{50} values of around 1 μM - except for compound **1**. Additional results following 72 h treatment of HeLa cells with compounds **2** and **4** showed IC_{50} values of 3.6 μM and 1.6 μM, respectively (Figure S40), displaying comparable potency to the *bis*-N-heterocyclic Ir compounds reported by Che *et al.*[15] Taken together, we thus identified four new Ir^{III}-NHC complexes with high anti-tumoral activities. It should be pointed out that the p53 tumor suppressor is mutated in approx. 50% of cancers and it is a major cause of tumor resistance. While the efficiency of platinum derivatives such as cisplatin and oxaliplatin is often reduced against cells having a deficient p53,[25] we found that our Ir-NHC complexes were highly cytotoxic against MDA-MB-231 which have a mutated p53. This is consistent with the observed anti-mitochondrial effect of compounds **1**–**5**, whose direct disruption of mitochondrial activity may cause p53 independent activation of apoptosis (see below).[5]

Cellular uptake and localization

Due to previous studies which showed structurally similar iridium compounds which localised to the mitochondria,[14,26] we investigated whether our compounds would show similar cellular distribution. Each of the molecules entered the cells and were highly visible by photo-luminescence (Figure 4), except compound **1**, which was poorly visible (Figure S41 of the Supplementary Information), in agreement with its poor cytotoxicity. The result of the co-localisation analysis were moderate to high Pearson correlation R values (measurement of the linear correlation between two variables, with limit value of 1 and 0 representing perfect co-localisation and absence of co-localisation, respectively) for the four toxic compounds compared to a relatively low value of 0.48 for the non-toxic compound **1**. This, along with their cytotoxicity, correlates with the calculated log$P_{o/w}$ values for the compounds as listed in Table 4, as higher hydrophobicity aids in traversing the mitochondrial membrane. This is thus consistent with reports showing the tendency of delocalised lipophilic cations, such as the molecules in the present study, to accumulate in the mitochondrial matrix due to the high membrane potential, in accordance with the Nernst equation.[27] Additionally, these results are in agreement with previous investigation showing higher cytotoxicity as compound's lipophilicity increases as reported by Lo,[28] Mao,[14] and Che[15]

3	1.33	0.85
4	1.58	0.84
5	2.05	0.90

Table 4. Partition coefficients log $P_{o/w}$ determined for complexes **1–5**.

Mitochondrial dysfunction

As the molecules were shown to localise to varying extents in the mitochondria, and as it was previously demonstrated that Pt^{II}-NHC complexes are able to disrupt mitochondrial function, we evaluated whether the cytotoxic activity of the NHC-Ir complexes was also correlated with mitochondrial dysfunctions as previously observed for NHC-Pt conjugates.[11f,29] To this end we measured mitochondrial superoxide production in the cells following treatment with two highly cytotoxic compounds, namely **2** and **4**, and one poorly toxic derivative (compound **1**) using MitoSOX™ red mitochondrial superoxide indicator. Additionally, a second experiment was carried out to determine the proportion of cells with actively respiring mitochondria via double staining with MitoTracker Deep Red (actively respiring mitochondria) and MitoTracker Green (all mitochondria), thus giving two distinct cell populations based on mitochondrial activity.[30]

Mitochondrial ROS induction

Mitochondrial reactive oxygen species (ROS) induction at sub-IC_{50} concentrations of the compounds was investigated using MitoSOX Red superoxide indicator, with staurosporine used as a positive control, as it is known to induce mitochondrial ROS.[31] Compounds **1** and **2** had no notable effect on ROS induction at low concentrations, while compound **4** was capable of inducing levels of ROS comparable to staurosporine (Figure 5). This is consistent with the higher observed mitochondrial localisation of compound **4** and indicates that it likely interferes with mitochondrial function upon entry. Such activity is in line with the anti-mitochondrial action of similar Ir^{III} complexes found in the literature.[14]

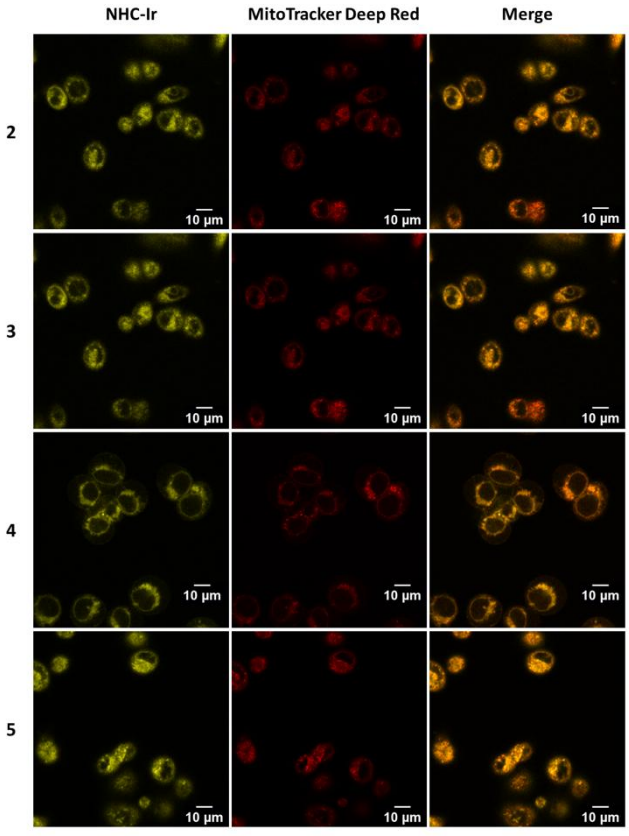

Figure 4. Confocal fluorescence microscopy of live HCT116 cells co-stained with 10 μM of each compound (90 min) and 500 nM MitoTracker Deep Red (30 min). Live cells were then maintained at 37°C and imaged immediately.

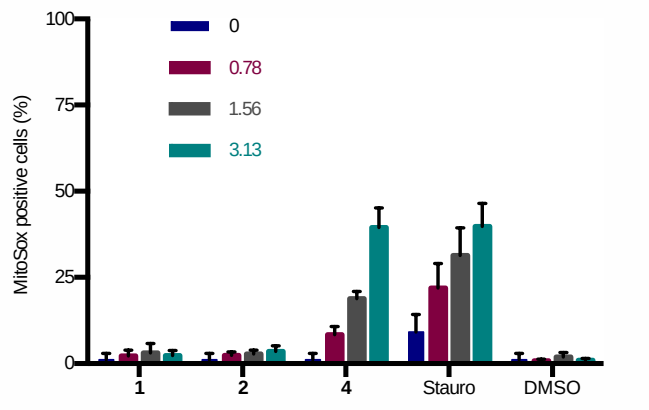

Figure 5. Percentage of MitoSox positive HCT116 cells following 24 hours treatment with each compound. Concentrations are in μM. Values are the mean of three independent experiments, with error bars representing one standard error of the mean, calculated using Prism software. Staurosporine = positive control. DMSO = vehicle control.

Mitochondrial respiratory activity

The second experiment to measure anti-mitochondrial activity relied on the ability to distinguish populations of cells with inactive mitochondria via double staining with MitoTracker Deep Red (labelling mitochondrial with an active membrane potential) and MitoTracker Green (labelling mitochondria independently of membrane potential). Carbonyl cyanide *m*-chlorophenyl hydrazine (CCCP) was chosen as a control for the MitoTracker Deep Red/Green assay as it is a known mitochondrial membrane potential decoupling agent.[32]

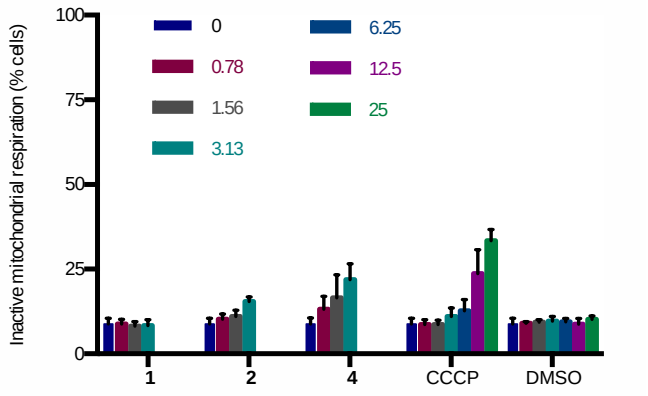

Figure 6. Percentage of HCT116 cells with inactive mitochondrial respiration following 24 hours treatment with compounds. Concentrations are in μM (and the equivalent vehicle quantities of DMSO). Values are the mean of three independent experiments, with error bars representing one standard error of the mean, calculated using Prism software. CCCP = positive control; DMSO = vehicle control.

Only compound **4** was capable of inducing notable loss of mitochondrial membrane potential at low micro-molar concentrations, with CCCP only doing so at higher concentrations (see Figure 6). Loss of mitochondrial membrane potential prevents ATP production and will eventually lead to the energy starvation of the cell, however it may more immediately lead to mitochondrial swelling followed by outer membrane rupture leading to cytochrome *c* release to the cytosol and induction of apoptosis.[33] This confirms the activity of compound **4** as a potent mitochondrial targeting compound, which may be explained by its higher lipophilicity and mitochondrial accumulation compared to compound **2**, despite similar IC_{50} values.

Cell death and apoptosis

To investigate further the mechanism of cell death induced by the NHC-Ir complexes, and as damaging of mitochondria may lead to activation of intrinsic apoptosis, we measured whether the cells entered apoptosis following 24 h treatment with sub-IC_{50} concentrations (Figure 7). While compound **1** remained mostly inactive as expected, compound **2** and **4** showed induction of early apoptosis at low μM concentrations. The similar IC_{50} value and induction of early-apoptosis of compound **2** and **4** despite the much lower level of mitochondrial disruption of compound **2** may be explained by its lower lipophilicity and mitochondrial localisation. Suggesting a potentially different mechanism of action between the two derivatives. As compound **4** showed a higher level of activity, its mechanism was further investigated.

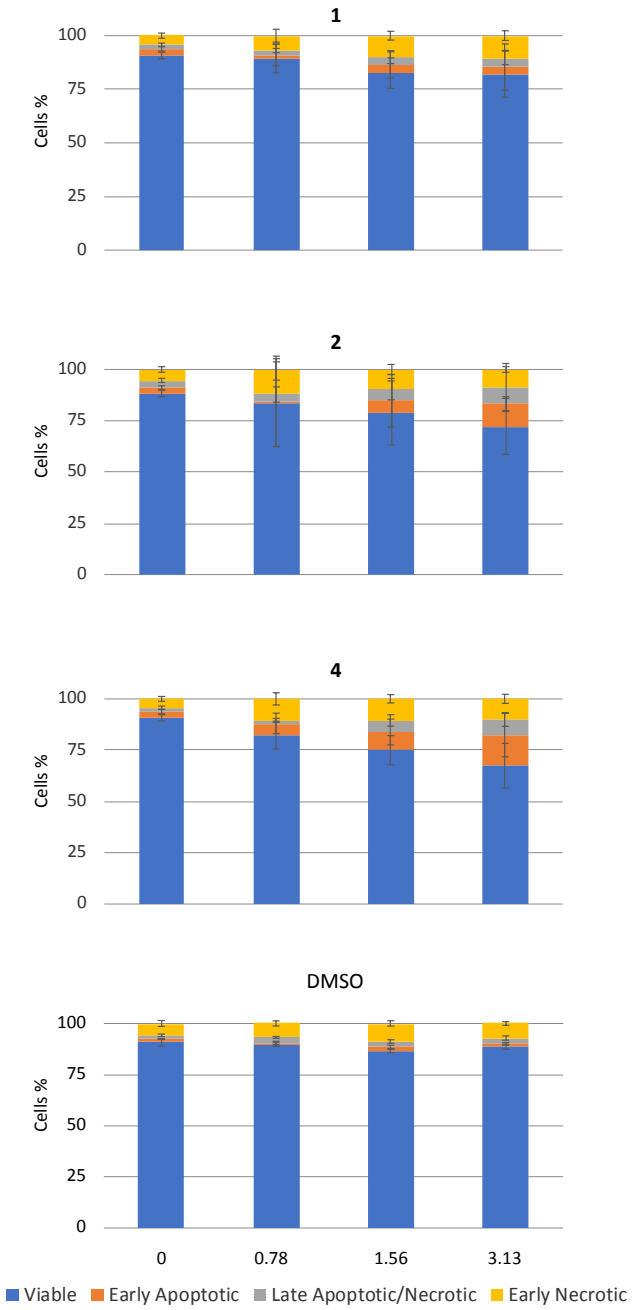

Figure 7. Annexin V (AnV)/ Propidium iodide (PI) analysis of HCT116 cells following 24 h treatment with the compounds. Viable cells = AnV-/PI-. Early apoptotic cells = AnV+/PI-. Late apoptotic/necrotic cells = AnV+/PI+. Early necrotic cells = AnV-/PI+. All values are the mean of three independent experiments ± one standard error of the mean.

In order to confirm whether the pathway of apoptotic induction by compound **4** was caspase dependant,[34] a luminescent caspase 3/7 activation assay was carried out at the IC_{50} concentration (Figure 8), with staurosporine used as positive control, as it is widely known to strongly induce apoptosis.[35] The result showed caspase 3/7 induction being roughly 60% that of staurosporine, confirming that compound **4** can induce strong activation of caspase 3/7 mediated apoptosis, which likely occurs due to direct activation of the intrinsic apoptotic pathway through mitochondrial disruption (Figure S42–S44).

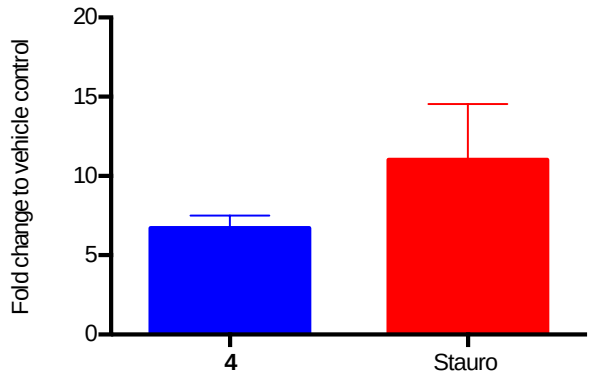

Figure 8. Induction of apoptosis shown by caspase 3/7 luminescence assay following 24 h treatment of HCT116 cells with 7.5 μM compound **4** and staurosporine. Results are expressed as the proportion of counted photons in the experimental condition to the counted photons of the DMSO vehicle control. Results are the mean of three independent experiments, with error bars representing one standard error of the mean.

Conclusions

The synthesis and characterization of a novel class of cationic Ir^{III} complexes featuring a pyridoannulated NHC as the ancillary ligand is herein presented. The compounds display interesting photophysical properties with a rare case of dual-emission arising from two close-lying excited states with mixed $^3MLCT_{C^N}/^3IL_{C^N}$ and mainly $^3LC_{NHC}$ character. The optical properties are combined with high tumor cell killing activities, making the investigated compounds potent theranostic agents with excellent cytotoxicity, as demonstrated by the IC_{50} values falling in the low μM regime.
Remarkably, the investigated Ir-NHC complexes display high cytotoxicity independently of the nature, either wild type or mutated, of the p53 tumor suppressor. The presented results are consistent with previous reports of delocalised lipophilic cationic metallodrugs, which are capable of localising to, and disrupting mitochondria, resulting in activation of apoptosis. A characteristic that play potentially a key-role in overcoming resistance to current anti-cancer therapeutics. A potent candidate is thus revealed for further studies and potential theranostic applications thanks to its combined optical and cytotoxicity properties.

Experimental Section

General considerations

$IrCl_3 \times nH_2O$ was purchased from Precious Metals Online. 2-phenylpyridine (ppy), 2-(2,4-difluorophenyl)pyridine (dfppy) and 2-phenylbenzothiazole (2-pbt) were purchased from Fluorochem and used as received without further purification. All procedures involving iridium complexes were carried out under argon atmosphere using standard Schlenk techniques. Silica gel for column chromatography was purchased from Sigma-Aldrich. NMR spectra were recorded using a Bruker Avance III HD 500 NMR spectrometer equipped with a N_2 cryo-probe CPPBBO Prodigy at 298 K. ^1H and $^{13}C\{^1H\}$ NMR spectra were calibrated to residual solvent signals. Partial assignment of protons and carbons' resonances have been made by means of COSY and HSQC spectra. Elemental analyses were obtained at the AMS Fédération de Chimie Le Bel, University of Strasbourg on a Flash 2000 ThermoFischer Scientific apparatus. High-resolution mass spectrometry was carried out on a MicroToF Bruker equipped with an electrospray ionization (ESI) source.

Synthesis

The pro-ligand [pyipy]PF_6,[17,36] 2′,6′-difluoro-2,3′-bipyridine (dfpypy),[37] 1-phenylisoquinoline (1-piq),[38] and the chloro-bridged iridium dimers[18] were synthetized accordingly to procedures reported elsewhere.

Synthesis of the [Ir(C^N)$_2$(pyipy)]PF_6 complexes: general procedure

A solution of CH_2Cl_2:CH_3OH 1:1 v/v was bubbled for 15 min before adding Ag_2O (2.5 equiv.) and 2-(2-pyridinyl)imidazo[1,5-*a*]pyridinium hexafluorophosphate (1 equiv.). The mixture was kept in the dark and refluxed for 18 hours under an argon atmosphere. Subsequently, the corresponding chloro-bridged Ir^{III} dimer $[Ir(\mu\text{-}Cl)(C^N)_2]_2$ (1 equiv.), where C^N denotes one of the five phenylpyridine-type of ligands employed, was added and the solution was stirred in the same conditions for 18 hours, then reaction mixture was cooled to room temperature and filtered over Celite plug. The volume of the solution was reduced and the compound precipitated with the help of a saturated aqueous solution of KPF_6. The solid was filtered and washed with water and Et_2O repeatedly. Compounds **4** and **5** were purified by silica gel column chromatography using CH_2Cl_2 as eluent. A mixture of CH_2Cl_2 with 0.2% of CH_3OH was used as TLC eluent mixture. R_f(**4**) = 0.3; R_f(**5**) = 0.5.

[Ir(dfpypy)$_2$(pyipy)]PF_6 (1). Yield 33%. ^{1}H NMR (500 MHz, 298 K, d_6-DMSO) δ: 9.04 (s, 1H, H_{5c}), 8.67 (d, J = 8.2 Hz, 1H, H_{6b}), 8.42 (t, J = 7.5 Hz, 1H), 8.30 (s, J = 3.5 Hz, 2H), 8.11 (dd, J = 13.8, 6.9 Hz, 2H), 8.02 (d, J = 5.4 Hz, 1H, H_{3b}), 7.89 (d, J = 5.1 Hz, 1H, H_{3a}), 7.77 (d, J = 5.4 Hz, 1H, H_{6a}), 7.67 (d, J = 9.4 Hz, 1H), 7.61–7.49 (m, 1H), 7.36–7.28 (m, 1H, H_{5b}), 7.28–7.22 (m, 1H, H_{5a}), 6.98 (dd, J = 18.4, 8.2 Hz, 2H, H_{2c}, H_{3c}), 6.69 (t, J = 6.7 Hz, 1H), 5.87 (s, 1H, $H_{5b'}$), 5.64 (s, 1H, $H_{5a'}$). $^{13}C\{^1H\}$ NMR (126 MHz, d_6-DMSO) δ: 186.2, 171.4, 164.0, 161.8, 161.8, 160.7, 160.6, 155.4, 153.0, 151.0, 143.4 (C_{6a}), 140.8, 140.3, 132.3, 126.7 (C_{5a}, C_{5b}), 126.5 (C_{2c}, C_{3c}), 125.6, 125.2, 124.4, 124.3, 124.1, 123.9, 119.7, 117.2 (C_{6b}), 115.4, 110.3 ($C_{5c'}$), 108.3 ($C_{5a'}$, $C_{5b'}$). $^{19}F\{^1H\}$ NMR (376 MHz, 298 K, CD_2Cl_2) δ: –67.22, –67.41, –68.83, –69.63. HR-ESI-MS calcd for $C_{32}H_{19}F_4IrN_7^+$ 770.12 ([M+H]$^+$); found 770.13. Anal for $C_{32}H_{19}F_{10}IrN_7P{\cdot}H_2O$: found C 41.66 H 2.44 N 9.97, calcd C 41.21 H 2.27 N 10.51.

[Ir(dfppy)$_2$(pyipy)]PF_6 (2). Yield 82%. ^{1}H NMR (500 MHz, 298 K, CD_2Cl_2) δ: 8.41 (s, 1H, H_{5c}), 8.39–8.34 (m, 2H), 8.29 (q, *J* = 8.0 Hz, 2H, H_{6b}), 7.91 (d, *J* = 5.2 Hz, 1H), 7.86 (dd, *J* = 14.4, 7.0 Hz, 2H), 7.72 (d, *J* = 5.7 Hz, 1H), 7.53 (t, *J* = 7.8 Hz, 2H, H_{3a}), 7.44 (t, *J* = 7.0 Hz, 1H), 7.09–7.04 (m, 2H), 7.00 (t, *J* = 6.7 Hz, 1H), 6.96–6.91 (m, 1H), 6.70–6.62 (m, 2H), 6.43 (t, *J* = 7.3 Hz, 1H), 5.96 (d, *J* = 2.3 Hz, 1H, $H_{5b'}$), 5.76 (dd, *J* = 7.8, 2.3 Hz, 1H, $H_{5a'}$). $^{13}C\{^1H\}$ NMR (126 MHz, 298 K, CD_2Cl_2) δ: 167.6, 167.3, 165.1, 165.1, 163.9, 163.9, 153.2, 150.3 (C_{3a}), 148.7, 142.4 (C_{6b}), 138.9, 138.3, 132.5, 125.6, 125.5, 124.3, 124.1, 124.0, 123.8, 123.6, 123.4, 119.0, 116.1, 114.4 ($C_{5b'}$, $C_{5a'}$), 113.3, 108.4 (C_{5c}), 99.8, 99.6, 99.4, 98.5, 98.3, 98.1. $^{19}F\{^1H\}$ NMR (376 MHz, 298 K, CD_2Cl_2) δ: –106.36, –106.51, –108.42, –108.84. HR-ESI-MS calcd for $C_{34}H_{21}F_4IrN_5^+$ 768.14 ([M+H]$^+$); found 768.13. Anal for $C_{34}H_{21}F_{10}IrN_5P{\cdot}2H_2O$: found C 42.60 H 2.43 N 7.22, calcd C 43.04 H 2.66 N 7.38.

[Ir(ppy)$_2$(pyipy)]PF_6 (3). Yield 82%. ^{1}H NMR (500 MHz, 298 K, CD_2Cl_2) δ: 8.32 (s, 1H, H_{5c}), 8.24–8.18 (m, 2H, H_{6b}), 7.99 (d, *J* = 8.1 Hz, 2H), 7.92 (d, *J* = 5.2 Hz, 1H), 7.84–7.78 (m, 4H), 7.74 (d, *J* = 6.4 Hz, 1H, H_{3a}), 7.56 (d, *J* = 5.8 Hz, 1H, H_{3b}), 7.48 (d, *J* = 9.5 Hz, 1H), 7.39–7.35 (m, 1H), 7.18–7.10 (m, 2H), 7.06 (td, *J* = 7.4, 1.2 Hz, 1H), 7.04–6.98 (m, 3H), 6.95 (ddd, *J* = 7.3, 5.9, 1.4 Hz, 1H, H_{2c}, H_{3c}), 6.87 (dd, *J* = 9.4, 6.4 Hz, 1H, $H_{3a'}$, $H_{3b'}$), 6.53 (d, *J* = 7.0 Hz, 1H, $H_{5b'}$), 6.34 (d, *J* = 6.7 Hz, 1H, $H_{5a'}$), 6.30–6.26 (m, 1H). $^{13}C\{^1H\}$ NMR (126 MHz, 298 K, CD_2Cl_2) δ: 170.6, 168.7, 167.3, 163.1, 153.5 (C_{3a}), 153.2, 150.5 (C_{3b}), 148.7, 147.2, 144.5, 143.0, 141.7, 137.9, 137.2, 132.3, 131.1($C_{5b'}$), 131.0 ($C_{5a'}$), 130.8, 130.4, 126.2, 125.2, 124.9, 124.9, 123.9 (C_{5b},C_{5a}), 123.2, 123.0, 121.9, 120.0, 119.7, 118.7, 115.2, 113.8, 107.8 (C_{5c}). HR-ESI-MS calcd for $C_{34}H_{25}IrN_5^+$ 696.17 ([M+H]$^+$); found 696.17. Anal for $C_{34}H_{25}F_6IrN_5P{\cdot}H_2O$: found C 47.08 H 2.97 N 8.01, calcd C 47.55 H 3.17 N 8.15.

[Ir(2-pbt)$_2$(pyipy)]PF_6 (4). Yield 66%. ^{1}H NMR (500 MHz, 298 K, CD_2Cl_2) δ: 8.33 (s, 1H, H_{5c}), 8.22 (dt, *J* = 12.7, 8.4 Hz, 2H), 8.00 (d, *J* = 4.1 Hz, 1H), 7.97–7.88 (m, 4H), 7.50 (dd, *J* = 9.5, 1.1 Hz, 1H), 7.41 (td, *J* = 7.8, 4.1 Hz, 3H), 7.23–7.13 (m, 4H), 7.03 (td, *J* = 7.4, 1.2 Hz, 1H), 6.97–6.87 (m, 3H), 6.57 (d, J = 7.6 Hz, 1H, $H_{5b'}$), 6.46 (d, J = 7.3 Hz, 1H, $H_{5a'}$), 6.32 (ddd, *J* = 7.5, 6.6, 1.1 Hz, 1H), 6.16 (d, *J* = 8.4 Hz, 1H, $H_{5b'}$), 6.10 (d, *J* = 8.4 Hz, 1H, $H_{5a'}$). $^{13}C\{^1H\}$ NMR (500 MHz, 298 K, CD_2Cl_2) δ: 182.8, 179.7, 167.0, 163.2, 153.9, 150.8, 149.6, 149.1, 147.3, 142.1, 140.7, 139.4, 132.8 ($C_{3b'}$), 132.7 ($C_{3a'}$), 132.3, 132.2, 131.8, 131.4, 131.3, 128.2, 127.9, 126.6, 126.5, 126.0, 125.8, 125.7, 125.2, 124.0, 123.9, 123.4, 122.5, 118.9, 118.0 ($C_{5b'}$), 117.5 ($C_{5a'}$), 115.8, 113.9, 108.0 (C_{5c}). HR-ESI-MS calcd for $C_{38}H_{25}IrN_5S_2^+$ 808.12 ([M+H]$^+$); found 808.11. Anal for $C_{38}H_{25}F_6IrN_5PS_2{\cdot}2H_2O$: found C 46.47 H 2.77 N 7.02, calcd C 46.15 H 2.96 N 7.08.

[Ir(1-piq)$_2$(pyipy)]PF_6 (5). Yield 35%. ^{1}H NMR (500 MHz, CD_2Cl_2, 298 K) δ: 9.00 (dd, J = 11.6, 6.8 Hz, 1H), 8.42 (d, J = 8.0 Hz, 1H), 8.38–8.33 (m, 1H), 8.26 (d, J = 8.3 Hz, 1H), 8.20 (t, J = 8.7 Hz, 1H), 7.98–7.91 (m, 1H), 7.85 – 7.80 (m, 2H), 7.73 (d, J = 5.4 Hz, 1H), 7.60 (d, J = 5.8 Hz, 1H), 7.47 (d, J = 9.5 Hz, 1H), 7.44 (d, J = 6.5 Hz, 1H), 7.34 (dd, J = 12.0, 6.0 Hz, 1H), 7.30 (d, J = 6.4 Hz, 1H), 7.26–7.20 (m, 1H), 7.03 (t, J = 7.3 Hz, 1H), 6.96 (t, J = 8.0 Hz, 1H), 6.84 (dd, J = 9.4, 6.4 Hz, 1H), 6.66 (d, J = 6.9 Hz, 1H), 6.53 (d, J = 7.7 Hz, 1H), 6.34 (d, J = 7.4 Hz, 1H), 6.22 (t, J = 6.9 Hz, 1H). $^{13}C\{^1H\}$ NMR (126 MHz, CD_2Cl_2, 298 K) δ: 171.34, 170.15, 168.05, 165.41, 153.43, 150.81, 150.36, 146.23, 145.00, 144.77, 141.68, 140.81, 136.87, 136.47, 132.44, 131.83, 131.74, 131.65, 131.49, 131.08, 130.92, 130.73, 130.29, 128.68, 127.40, 127.32, 127.23, 126.72, 126.48, 126.25, 125.20, 123.95, 122.95, 122.40, 121.61, 121.56, 118.67, 115.11, 113.90, 107.85. HR-ESI-MS calcd for $C_{42}H_{29}IrN_5^+$ 796.20 ([M+H]$^+$); found 796.20. Anal for $C_{42}H_{29}F_6IrN_5P{\cdot}4H_2O$: found C 49.00 H 3.13 N 6.41, calcd C 49.80 H 3.68 N 6.91.

X-ray diffractometric analysis

The crystals of compound **3** were placed in oil, and a single crystal was selected, mounted on a glass fibre and placed in a low-temperature N_2 stream. X-ray diffraction data collection was carried out on a Bruker APEX II DUO Kappa-CCD diffractometer equipped with an Oxford Cryosystem liquid N_2 device, using Mo-Kα radiation (λ = 0.71073 Å). The crystal-detector distance was 38 mm. The cell parameters were determined (APEX3 software)[39] from reflections taken from three sets of 6 frames, each at 10s exposure. The structure was solved using the program SHELXT-2014.[40] The refinement and all further calculations were carried out using SHELXL-2014.[41] The H-atoms were included in calculated positions and treated as riding atoms using SHELXL default parameters. The non-H atoms were refined anisotropically, using weighted full-matrix least-squares on F^2. A semi-

empirical absorption correction was applied using SADABS in APEX3.[39] The atoms F(3), F(4), F(5), F(6) of the hexafluorophosphate group are disordered over two positions. CCDC 1983105 for compound **3**.

Photophysical characterization

Instrument details. Absorption spectra were measured on a Varian Cary 100 double-beam UV–VIS spectrophotometer and baseline corrected. Steady-state emission spectra were recorded on a Horiba Jobin−Yvon IBH FL-322 Fluorolog 3 spectrometer equipped with a 450 W xenon arc lamp, double-grating excitation, and emission monochromators (2.1 nm mm^{-1} of dispersion; 1200 grooves mm^{-1}) and a Hamamatsu R13456 red sensitive Peltier-cooled PMT detector. Emission and excitation spectra were corrected for source intensity (lamp and grating) and emission spectral response (detector and grating) by standard correction curves. Time-resolved measurements were performed using either the time-correlated single-photon counting (TCSPC) or the Multi-Channel Scaling (MCS) electronics option of the TimeHarp 260 board installed on a PicoQuant FluoTime 300 fluorimeter (PicoQuant GmbH, Germany), equipped with a PDL 820 laser pulse driver. A pulsed laser diode LDH-P-C-375 (λ = 375 nm, pulse full width at half maximum FWHM <50 ps, repetition rate 200 kHz–40 MHz) was used to excite the sample and mounted directly on the sample chamber at 90°. The photons were collected by a PMA Hybrid-07 single photon counting detector. The data were acquired by using the commercially available software EasyTau II (PicoQuant GmbH, Germany), while data analysis was performed using the built-in software FluoFit (PicoQuant GmbH, Germany). All the solvents were spectrophotometric grade. Deaerated samples were prepared by the freeze-pump-thaw technique by using a homemade quartz cuvette equipped with a Rotaflo® stopcock. To rule out the possible origin of the bi-exponential decays as due to any trace impurities, crystalline samples were used to prepare the solutions for spectroscopical investigation.

Methods. For time resolved measurements, data fitting was performed by employing the maximum likelihood estimation (MLE) method. The quality of the fit was assessed by inspection of the reduced χ^2 function and of the weighted residuals. For multi-exponential decays, the intensity, namely *I*(t), has been assumed to decay as the sum of individual single exponential decays (Eqn. 1):

$$I(t) = \sum_{i=1}^{n} \alpha_i exp\left(-\frac{t}{\tau_i}\right) \qquad Eqn. 1$$

where τ_i are the decay times and α_i are the amplitude of the component at t = 0. In the tables, the percentages to the pre-exponential factors, α_i, are listed upon normalization.

Luminescence quantum yields were measured in optically dilute solutions (optical density <0.1 at the excitation wavelength) and compared to reference emitter by following the method of Demas and Crosby.[42] Quinine sulphate in 0.5 M H_2SO_4 (PLQY = 0.55)[43] and the $Ru(bpy)_3Cl_2$ complex in air-equilibrated water solution at room temperature (PLQY = 0.04)[44] were used as reference standard for complexes **1** and **2**–**5**, respectively.

Computational details

The structures of the complexes **1**–**5** in the electronic ground state have been fully optimized at the DFT/B3LYP[45] level of theory using essentially double-ζ basis sets including scalar relativistic effects for all atoms.[46] The use of triple-ζ basis sets does not modify drastically the results obtained for complex **2** (systematic ~10 nm red-shift of the singlet transitions; Figure S13). This justifies the use of double-ζ basis sets for the large systems, which could not be handled otherwise. The calculations have been performed in CH_2Cl_2 within the COSMO (conductor-like-screening model) model.[47] The absorption spectra have been computed at the TD-DFT level (80 roots) including spin-orbit effects at the perturbation level of theory within the zero-order relativistic approximation (ZORA).[48] The structures of the low-lying triplet excited states T_n (n = 1–4) have been optimized at the same level of theory using the Tamm-Dancoff approximation (TDA) in order to avoid triplet instability problems.[49] The calculations have been performed with the ADF *2019* package (ADF, SCM, Theoretical Chemistry, Vrije Universiteit, Amsterdam, The Netherlands https://www.scm.com/doc/ADF/index.html).

Biological tests

Storage of compounds

All tested compounds were stored as 5 mM stock solutions in DMSO at 4°C. Prior to use, stocks were heated and sonicated briefly at 37°C in a bath sonicator. Prior to treatment of cells, stock compounds were diluted to desired concentrations in the culture medium RPMI 1640 medium containing 10% ($^v/_v$) fetal bovine serum (FBS, Sigma-Aldrich), Penicillin-Streptomycin (10U-0.1 mg, Sigma-Aldrich).

Cell culture and treatment conditions

HCT116 (Human colorectal carcinoma, CCL-247™) and MDA-MB-231 (Human breast cancer cell line, HTB-26™) cells were obtained from American Type Culture Collection (ATCC®). Cells were maintained in RPMI 1640 (Roswell Park Memorial Institute, Sigma-Aldrich) medium containing 10% (v/v) FBS, Penicillin-Streptomycin (P/S; 10U/0.1 mg) in a 37°C, 80% humidity and 5% CO_2 incubator. Once confluence reached ~80%, cultures were maintained by removal of spent culture medium and twice washing with PBS, followed by treatment with trypsin-EDTA (5mg mL^{-1} : 2 mg mL^{-1}; Sigma) for 5 min at 37°C, collection of cells and re-seeding in a new T75 culture flask. For treatment with tested compounds, HCT116 cells were seeded at 24000 cells and MDA-MB-231 cells at 20,000 cells per well in treated flat-bottom 96 well culture plates (Greiner CELLSTAR®) prior to treatment with the tested compounds the following day. Treatment was applied by aspiration of culture medium from wells and replacement with the desired dilutions of the compounds.

Cellular uptake and localization

Determination of log $P_{o/w}$

The octanol-water partition coefficient (log $P_{o/w}$) for complexes **1–5** were determined using the shake-flask method. Stock solutions of the compounds were prepared in a mixture of water and 1-octanol 50/50 $^{V}/_{V}$ (total complex concentration 3×10^{-5} M). The resultant solutions were shaken for 48 hours and then equilibrated for 24 hours. The partition coefficients were determined using UV absorbance spectroscopy. Log$P_{o/w}$ was defined as the logarithm of the ratio of the concentrations of the complex in the organic and aqueous phases as by the following equation (Eqn. 2):

$$\boldsymbol{logP_{o/w} = log\left\{\frac{[complex(octanol)]}{[complex(water)]}\right\}} \qquad \boldsymbol{Eqn.2}$$

where [complex(octanol)] and [complex[water] are the concentration of the complex under investigation in 1-octanol and water, respectively.

Mitochondrial co-localisation

HCT116 cells were seeded at 80,000 in 35 mm µ-Dishes (IBIDI) in 600 µL RPMI (+10% FBS + P/S). The following day, medium was removed from the cells and replaced with 600 µL RPMI culture medium containing 10 µM of one of the compounds and was then incubated for 1 h 30 min at 37°C. The medium was then removed and replaced with 500 nM MitoTracker Deep Red in serum-free and phenol-red free DMEM medium and incubated at 37°C for 30 min. The medium was then aspirated and replaced with 1 mL phenol-red free DMEM, with the cells then imaged using a Leica DMI4000. All iridium compounds were excited using a 405 nm laser and collected as follows: compound **1**: 420–550 nm; compound **2**: 450–550 nm; compound **3**: 475–575 nm; compound **4**: 550–600 nm; compound **5**: 600–675 nm. MitoTracker Deep Red was excited using a 635 nm laser and collected at 650-700 nm. The overlapping emission spectra of compound **5** and MitoTracker Deep Red was not of concern due to their non-overlapping excitation spectra. Orthogonal excitation of the two compounds allow collection the emission of compound **5** and MitoTracker Deep Red independently.

Cytotoxicity assay

Cell metabolic activity was measured by using an MTS (3-(4,5-dimethylthiazol-2-yl)-5-(3-carboxymethoxyphenyl)-2-(4-sulfophenyl)-2H-tetrazolium) assay (CellTiter 96® AQueous One Solution Cell Proliferation Assay, Promega). MTS is a colorimetric reagent which undergoes color change in the presence of NAD(P)H, which is proportional to metabolic activity. Following treatment for the desired length of time, MTS reagent was added according to the manufacturer's instructions, followed by incubation at 37°C for 30-60 min (until significant colour change was observed). Plates were read at 490 nm (reagent absorbance) and 700 nm (background)(SP200, Safas Monaco). Results were expressed by the subtraction of background absorbance and expression of viability relative to non-treated controls (considered as 100% viability). The percentage of viability was calculated using the following equation (eqn. 3):

$$\boldsymbol{\%\ viability = \left[\frac{OD(treatment)}{OD(100\%\ viability)} \times 100\right]} \qquad \boldsymbol{Eqn.3}$$

Annexin V/Propidium iodide assay

Cell death and apoptosis were investigated by double staining with Annexin V, a protein which binds to phosphatidylserine, an inner leaflet membrane phospholipid which is externalised during apoptosis, and propidium iodide (PI), a membrane impermeable DNA intercalating agent that enters cells which have lost membrane integrity, and fluoresces only when bound to nucleic acids. Following treatment, the cells were recovered via trypsinisation, and washed in Annexin V binding buffer (10 mM HEPES, 140 mM NaCl, 2.5 mM $CaCl_2$, pH 7.3-7.4). Triplicates were pooled and stained with FITC-conjugated Annexin V (eBioscience) diluted 1/100 with prepared Annexin V binding buffer which was incubated for 15 min at room temperature sheltered from light. Cells were washed with Annexin V binding buffer and transferred to tubes containing 15 µM propidium iodide (Sigma Aldrich), which were analysed immediately via flow cytometry (FACSCalibur™, Becton Dickinson). Data were analysed using FlowJo software.

Caspase 3/7 activation assay

Caspase 3/7 activation was investigated using the Caspase-Glo® 3/7 Assay System (Promega), which functions via a proluminescent caspase-3/7 DEVD-aminoluciferin substrate, thus generating processible luciferase substrate, and luminescence, proportional to caspase 3/7 activity. Following treatment, 100 µL reagent was added to each well, which were then mixed by vigorous pipetting. After 30 min incubation at room temperature cell-lysate was transferred to an opaque 96 well plate, with luminescence then read using a Safas Monaco plate reader.

Mitochondrial dysfunction analysis

The effects of the tested compounds on mitochondrial superoxide production and respiratory activity were evaluated using flow cytometry assays. Following treatment, cells were harvested and washed with Hank's Balanced Salt Solution (HBSS)(Sigma-Aldrich) before incubation with MitoSOX Red

mitochondrial superoxide indicator (1 μM, Invitrogen)(a mitochondrial targeted molecule which fluoresces upon reaction with superoxide radical), diluted in HBSS, in the dark for 30 minutes at 37°C. For the second assay, cells were stained with MitoTracker Green FM (labelling all mitochondria) and MitoTracker Deep Red FM (labelling mitochondria with an active membrane potential)(0.2 μM, Invitrogen) and incubated in the same manner. Cells were then washed with HBSS and analysed via flow cytometry in the same manner as the Annexin V/Propidium iodide assay using the appropriate fluorescence channels.

Acknowledgments

A.B. and M.M. gratefully acknowledge the Université de Strasbourg and CNRS for financial support. The International Centre for Frontier Research in Chemistry (icFRC), and the Labex CSC (ANR-10-LABX-0026 CSC) within the Investissement d'Avenir program ANR-10-IDEX-0002-02 is also acknowledged for funding the PhD fellowship of A.B. M.M. kindly acknowledges the French Agence Nationale de Recherche (ANR) for the grant ANR-18-CE06-007-01. C.McC. was a recipient of a PhD grant from the French Ministère de l'Education Nationale, de la Recherche et de la Technologie This work was also financially supported by an Idex Interdisciplinaire (CF/PN/CB/N°2017-973-5). Lastly, we would like to thank Anais Brion and the quantitative imaging platform at the faculty of pharmacy, Strasbourg, for their aid with the confocal microscopy experiments.

Keywords: anticancer agents • iridium • density functional theory • metallodrugs • phosphorescence

[1] C. Monneret, *Ann. Pharm. Fran.* **2011**, *69*, 3523.
[2] E. Martinez-Balibrea, A. Martínez-Cardús, A. Ginés, V. Ruiz de Porras, C. Moutinho, L. Layos, J. L. Manzano, C. Bugés, S. Bystrup, M. Esteller, A. Abad, *Mol. Caner Ther.* **2015**, *14*, 1767.
[3] W. Hu, J. J. Kavanagh, *Lancet Oncol.* **2003**, *4*, 721.
[4] a) A. Erxleben, *Curr. Med. Chem.* **2019**, *26*, 694; b) V. Gogvadze, S. Orrenius, B. Zhivotovsky, *Apoptosis* **2009**, *14*, 624; c) S. Fulda, L. Galluzzi, G. Kroemer, *Nat. Rev. Drug Discovery* **2010**, *9*, 447.
[5] P. V. Simpson, N. M. Desai, I. Casari, M. Massi, M. Falasca, *Future Med. Chem.* **2019**, *11*, 119.
[6] a) K. K.-W. Lo, K. Y. Zhang, *RSC Adv.* **2012**, *2*, 12069; b) C.-H. Leung, H.-J. Zhong, D. S.-H. Chan, D.-L. Ma, *Coord. Chem. Rev.* **2013**, *257*, 1764; c) C. Caporale, M. Massi, *Coord. Chem. Rev.* **2018**, *363*, 71; d) Lo (Ed.), *Luminescent and photoactive transition metal complexes as biomolecular probes and cellular reagents*, *Struct. Bonding.*, 165, Springer, **2015**.
[7] a) G. Bertrand, *J. Organomet. Chem.* **2005**, *690*, 5397; b) R. H. Crabtree, *Coord. Chem. Rev.* **2007**, *251*, 595; c) F. Glorius, *Top. Organomet. Chem.* **2007**, *21*, 47; d) S. P. Nolan (Ed.), in *N-Heterocyclic Carbenes in Synthesis*; Wiley-VCH: Weinheim, Germany, **2006**; e) W. A. Herrmann, C. Köcher, *Angew. Chem. Int. Ed. Engl.* **1997**, *36*, 2162; f) V. César, S. Bellemin-Laponnaz, L. H. Gade, *Chem. Soc. Rev.* **2004**, *33*, 619; g) W. A. Herrmann, L. J. Goossen, G. R. J. Artus, C. Köcher, *Chem. Rev.* **2014**, *114*, 8747; h) M. N. Hopkinson, C. Richter, M. Schedler, F. Glorius, *Nature* **2014**, *510*, 485.
[8] a) A. Igau, H. Grutzmacher, A. Baceiredo, G. Bertrand, *J. Am. Chem. Soc.* **1988**, *110*, 6463; b) A. J. Arduengo, R. L. Harlow, M. Kline, *J. Am. Chem. Soc.* **1991**, *113*, 361; c) D. Bourissou, O. Guerret, F. P. Gabbaï, G. Bertrand, *Chem. Rev.* **2000**, *100*, 39.
[9] a) E. Peris, *Chem. Rev.* **2018**, *118*, 9988; b) F. Glorius (Ed.) *in N-Heterocyclic Carbenes in Transition Metal Catalysis*; Springer-Verlag: Berlin, **2007**.
[10] a) A. Bonfiglio, M. Mauro, *Eur. J. Inorg. Chem.* **2020**, 3427; b) C. A. Smith, M. R. Narouz, P. A. Lummis, I. Singh, A. Nazemi, C.-H. Li, C. M. Crudden, *Chem. Rev.* **2019**, *119*, 4986; c) R. Visbal, M. C. Gimeno, *Chem. Soc. Rev.* **2014**, *43*, 3551; d) L. Mercs, M. Albrecht, *Chem. Soc. Rev.* **2010**, *39*, 1903; e) M. Albrecht, *Chimia* **2010**, *64*, 184; f) B. M. Nelson, A. G. Tennyson, C. W. Biewlaski, *J. Phys. Org. Chem.* **2012**, *25*, 531.
[11] For some selected examples of metallodrugs containing NHC ligands see: a) Y. Gothe, T. Marzo, L. Lessori, N. Metzler-Nolte, *Chem. Eur. J.* **2016**, *22*, 12487; b) F. Schmitt, K. Donnelly, J. K. Muenzner, T. Rehm, V. Novohradsky, V. Brabec, J. Kasparkova, M. Albrecht, R. Schobert, T. Mueller, *J. Inorg. Biochem.* **2016**, *163*, 221; c) T.-L. Lam, K.-C. Tong, C. Yang, W.-L. Kwong, Z. Guan, M.-D. Li, V. K.-T. Lo, S. L-F. Chan, D. L. Phillips, C.-N. Lok, C.-M. Che, *Chem. Sci.* **2019**, *10*, 293; d) Z. Xu, Y. Zhang, S. Zhang, X. Jia, G. Zhong, Y. Yang, Q. Du, J. Li, Z. Liu, *Cancer Lett*. **2019**, *447*, 75; e) J. Zhang, J. Liu, Z. Liu, B. Liu, S. Song, X. He, C. Che, M. Si, G. Yang, Z. Liu, *J. Inorg. Biochem.* **2020**, *207*, 111063; f) N. Chekkat, G. Dahm, E. Chardon, M. Wantz, J. Sitz, M. Decossas, O L. Lambert, B. Frisch, R. Rubbiani, G. Gasser, G. Guichard, S. Fournel, S. Bellemin-Laponnaz, *Bioconjug. Chem.* **2016**, *27*, 1942.
[12] For some selected reviews see: a) M. Skander, P. Retailleau, B. Bourrié, L. Schio, P. Mailliet, A. Marinetti, *J. Med. Chem.* **2010**, *53*, 2146; b) S. Bellemin-Laponnaz, *Eur. J. Inorg. Chem.* **2020**, 10; c) F. Cisnetti, A. Gautier, *Angew. Chem. Int. Ed.* **2013**, *52*, 11976; d) W. Liu, R. Gust, *Chem. Soc. Rev.* **2013**, *42*, 755; e) W. Liu, R. Gust, *Coord. Chem. Rev.* **2016**, *329*, 191.
[13] a) L. Benhamou, E. Chardon, G. Lavigne, S. Bellemin-Laponnaz, V. César, *Chem. Rev.* **2011**, *111*, 2705; b) J. C. Y. Lin, R. T. W. Huang, C. S. Lee, A. Bhattacharyya, W. S. Hwang, I. J. B. Lin, *Chem. Rev.* **2009**, *109*, 3561; c) A. A. Danopoulos, T. Simler, P. Braunstein, *Chem. Rev.* **2019**, *119*, 3730; d) D. G. Gusev, *Organometallics* **2009**, *28*, 6458; e) D. J. Nelson, S. P. Nolan, *Chem. Soc. Rev.* **2013**, *42*, 6723; f) S. Diez-Gonzalez, S. P. Nolan, *Coord. Chem. Rev.* **2007**, *251*, 874; g) H. V. Huynh, *Chem. Rev.* **2018**, *118*, 9457.
[14] a) Y. Li, C.-P. Tan, W. Zhang, L. He, L.-N. Ji, Z.-W. Mao, *Biomaterials* **2015**, *29*, 95; b) Y. Li, K.-N. Wang, L. He, L.-N. Ji, Z.-W. Mao, *J. Inorg. Biochem.* **2020**, *205*, 110976.
[15] C. Yang, F. Mehmood, T. L. Lam, S. L.-F. Chan, Y. Wu, C.-S. Teung, Z. Guan, K. Li, C. Y.-S. Chung, C.-Y. Zhou, T. Zou, C.-M. Che, *Chem. Sci.* **2016**, *7*, 3123.
[16] a) Z. Tian, Y. Yang, L. Guo, G. Zhong, J. Li, Z. Liu, *Inorg. Chem. Front.* **2018**, *5*, 3106; b) Y. Yang, L. Guo, Z. Ge, Z. Tian, Y. Gong, H. Zheng, Q. Du, X. Zheng, Z. Liu, *Dyes Pigm.*, **2019**, *161*, 119.
[17] M. Alcarazo, S. J. Roseblade, A. R. Cowley, R. Fernández, J. M. Brown, J. M. Lassaletta, *J. Am. Chem. Soc.* **2005**, *127*, 3290.
[18] M. Nonoyama, *Bull. Chem. Soc. Jpn.* **1974**, *47*, 767.

[19] a) S. Lamansky, P. Djurovich, D. Murphy, F. Abdel-Razzaq, R. Kwong, I. Tsyba, M. Bortz, B. Mui, R. Bau, M. E. Thompson, *Inorg. Chem.* **2001**, *40*, 1704; b) T. Yutaka, S. Obara, S. Ogawa, K. Nozaki, N. Ikeda, T. Ohno, Y. Ishii, K. Sakai, M. Haga, *Inorg. Chem.* ***2005***, *44*, 4737; c) F. De Angelis, S. Fantacci, N. Evans, C. Klein, S. M. Zakeeruddin, J.-E. Moser, K. Kalyanasundaram, H. J. Bolink, M. Grätzel, M. K. Nazeeruddin, *Inorg. Chem.* **2007**, *46*, 5989.

[20] a) S. Lamansky, P. Djurovich, D. Murphy, F. Abdel-Razzaq, H.-E. Lee, C. Adachi, P. E. Burrows, S. R. Forrest, M. E. Thompson, *J. Am. Chem. Soc.* **2001**, *123*, 4304; b) F. Monti, F. Kessler, M. Delgado, J. Frey, F. Bazzanini, G. Accorsi, N. Armaroli, H. J. Bolink, E. Ortí, R. Scopelliti, Md. K. Nazeeruddin, E. Baranoff, *Inorg. Chem.* **2013**, *52*, 10292; c) F. Kessler, R. D. Costa, D. Di Censo, R. Scopelliti, E. Ortí, H. J. Bolink, S. Meier, W. Sarfert, M. Grätzel, Md. K. Nazeeruddina, E. Baranoff, *Dalton Trans.* **2012**, *41*, 180; d) C.-H. Yang, J. Beltran, V. Lemaur, J. Cornil, D. Hartmann, W. Sarfert, R. Fröhlich, C. Bizzarri, L. De Cola, *Inorg. Chem.* **2010**, *49*, 9891.

[21] Samples for photophysical investigation were prepared starting from crystalline materials thus to rule out the presence of impurities as the origin of the dual emission.

[22] a) A. K. Pal, S. Krotkus, M. Fontani, C. F. R. Mackenzie, D. B. Cordes, A. M. Z. Slawin, I. D. W. Samuel, E. Zysman-Colman, *Adv. Mater.* **2018**, 1804231; b) S. Ladouceur, L. Donato, M. Romain, B. P. Mudraboyina, M. B. Johansen, J. A. Wisner, E. Zysman-Colman, *Dalton Trans.* **2013**, *42*, 8838; c) Y.-S. Yeh, Y.-M. Cheng, P.-T. Chou, G.-H. Lee, C.-H. Yang, Y. Chi, C.-F. Shu, C.-H. Wang, *ChemPhysChem* **2006**, *7*, 2294; d) D. N. Kozhevnikov, V. N. Kozhevnikov, M. Z. Shafikov, A. M. Prokhorov, D. W. Bruce, J. A. G. Williams, *Inorg. Chem.* **2011**, *50*, 3804; e) Y. You, Y. Han, Y.-M. Lee, S. Y. Park, W. Nam, S. J. Lippard, *J. Am. Chem. Soc.* **2011**, *133*, 11488.

[23] A. Bonfiglio, K. Magra, C. Cebrián, F. Polo, P. C. Gros, P. Mercandelli, M. Mauro, *Dalton Trans.* **2020**, *49*, 3102.

[24] C. Gourlaouen, J. Eng, M. Otsuka, E. Gindenperger, C. Daniel, *J. Chem. Theor. Comput.* **2015**, *11*, 99.

[25] F. Toscano, B. Parmentier, Z. El Fajoui, Y. Estornes, J.-A. Chayvialle, J.-C. Saurin, J. Abello, *Biochem. Parmacol.* **2007**, *74*, 392.

[26] A. Zamora, G. Vigueras, V. Rodríguez, M. D. Santana, J. Ruiz, *Coord. Chem. Rev.* **2018**, *360*, 34.

[27] R. A. J. Smith, R. C. Hartley, M. P. Murphy, *Antiox. Redox Signal.* **2011**, *15*, 3021.

[28] P. K. Lee, H.-W. Liu, S.-M. Yiu, M.-W. Louie, K. K.-W. Lo, *Dalton Trans.* **2011**, *40*, 2180.

[29] M. Wantz, M. Bouché, G. Dahm, N. Chekkat, S. Fournel, S. Bellemin-Laponnaz, *Int. J. Mol. Sci.* **2018**, *19*, 3472.

[30] R. Zhou, A. S. Yazdi, P. Menu, J. Tschopp, *Nature* **2011**, *469*, 221.

[31] I. Kruman, Q. Guo, M. P. Mattson, *J. Neurosci. Res.* **1998**, *51*, 293.

[32] C. E. Ganote, S. A. Armstrong, *J. Mol. Cell Cardiol.* **2003**, *35*, 749.

[33] a) D. Safiulina, V. Veksler, A. Zharkovsky, A. Kaasik, *J. Cell. Physiol.* **2006**, *206*, 347; b) P. X. Petit, M. Goubern, P. Diolez, S. A. Susin, N. Zamzani, G. Kroemer, FEBS Lett. **1998**, *426*, 111.

[34] J. Li, J. Yuan, *Oncogene* **2008**, *27*, 6194.

[35] R. Bertrand, E. Solary, P. O'Connor, K. W. Kohn, Y. Pommier, *Exp. Cell Res.* **1994**, *211*, 314.

[36] a) J. T. Hutt, Z. D. Aron, *Org. Lett.* **2011**, *13*, 5256; b) K. Magra, M. Darari, E. Domenichini, A. Francés-Monerris, C. Cebrián, M. Beley, M. Pastore, A. Monari, X. Assfeld, S. Haacke, P. C. Gros, *J. Phys. Chem. C* **2020**, *124*, 18379.

[37] S. J. Lee, K.-M. Park, K. Yang, Y. Kang, *Inorg. Chem.* **2009**, *48*, 1030.

[38] Y.-J. Su, H.-L. Huang, C.-L. Li, C.-H. Chien, Y.-T. Tao, P.-T. Chou, S. Datta, R.-S. Liu, *Adv. Mater.* **2003**, *15*, 884.

[39] M86-EXX229V1 APEX3 User Manual, Bruker AXS Inc., Madison, USA, **2016**.

[40] G. M. Sheldrick, *Acta Cryst.* **2015**, A71, 3-8.

[41] G. M. Sheldrick, *Acta Cryst.* **2015**, C71, 3-8.

[42] a) G. A. Crosby, J. N. C. Demas, *J. Am. Chem. Soc.* **1970**, *92*, 7262; b) H. Ishida, J.-C. Bünzli, A. Beeby, *Pure Appl. Chem.* **2016**, *88*, 701–711; c) C. Würth, M. Grabolle, J. Pauli, M. Spieles, U. Resch-Genger, *Nat. Prot.* **2013**, *8*, 1535.

[43] a) A. M. Brouwer, *Pure Appl. Chem.* **2011**, *83*, 2213; b) L. Porrès, A. Holland, L. O. Palsson, A. P. Monkman, C. Kemp, A. Beeby. *J. Fluoresc.* **2006**, *16*, 267.

[44] I. Ishida, S. Tobita, Y. Hasegawa, R. Katoh, K. Nozaki, *Coord. Chem. Rev.* **2010**, *254*, 2449.

[45] P. J. Stephens, F. J. Devlin, C. F. Chabalowski, M. J. Frisch, *J. Phys. Chem.* **1994**, *98*, 11623.

[46] E. Van Lenthe, E. J. Baerends, *J. Comput. Chem.* **2002**, *24*, 1142.

[47] A. Klamt, *J. Phys. Chem.* **1995**, *99*, 2224.

[48] a) E. van Lenthe, R. van Leeuwen, E. J. Baerends, J. G. Snijders, *Int. J. Quant. Chem.* **1996**, *57*, 281; b) F. Wang, T. Ziegler, *J. Chem. Phys.* **2005**, *123*, 154102; c) F. Wang, T. Ziegler, E. van Lenthe, S. van Gisbergen, E. J. Baerends, *J. Chem. Phys.* **2005**, *122*, 204103.

[49] M. J. G. Peach, D. J. Tozer, *J. Phys. Chem. A* **2012**, *116*, 9783.

A novel class of phosphorescent Ir-N-heterocyclic carbene metallodrugs is investigated that preferentially target mitochondria. The complexes possess high cytotoxicity against cancer cell lines via mitochondrial dysfunctioning activity and effectively induce reactive oxygen species production, make them potent theranostic agents.

Iridium-NHC complexes as theranostic agents

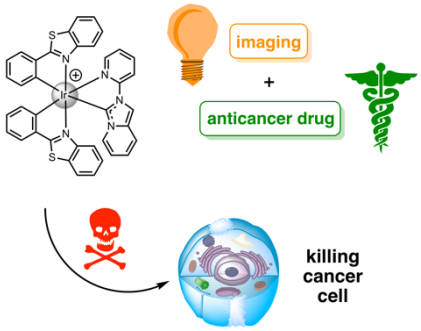

Theranostic agents

*Anna Bonfiglio, Conor McCartin, Ulises Carrillo, Cristina Cebrián, Philippe C. Gros, Sylvie Fournel, Antoine Kichler, Chantal Daniel, and Matteo Mauro**

Page No. – Page No.

Ir^{III}-pyridoannelated N-heterocyclic carbene complexes: potent theranostic agents via mitochondria targeting